Towards lower annealing temperatures and enhanced functional properties in aerosol-deposited piezoelectric thick films: A study of the effect of Li additive on BaTiO3 films

Anass Chrir, Oscar Rojas, Maggy Colas, Laurence Boyer, Olivier Durand, Pascal Marchet

Towards lower annealing temperatures and enhanced functional properties in aerosol-deposited piezoelectric thick films: a study of the effect of Li additive on $BaTiO_3$ films

Anass Chrir[a,*], Oscar Rojas[b], Maggy Colas[a], Laurence Boyer[b], Olivier Durand[b], Pascal Marchet[a]

[a] Univ. Limoges, CNRS, IRCER, UMR 7315, F-87000 Limoges, France
[b] Center for Technology Transfers in Ceramics (CTTC), 7 rue Soyouz, 87068, Limoges, France

*Corresponding author: Anass Chrir
Email address: anass.chrir@unilim.fr
Full postal address: Centre Européen de la Céramique, 12 Rue Atlantis, 87068 Limoges, France

Abstract

The effect of incorporating Li additive (Li_2CO_3) into aerosol deposited $BaTiO_3$ thick films was investigated. The addition of Li_2CO_3 to the deposited powder facilitated grain growth during post deposition process, even for low annealing temperatures (≤ 700 °C). Therefore, this additive decreased the threshold for ferro/piezoelectricity recovery from 800 °C to 650 °C. Furthermore, annealing at temperatures ≥ 800 °C yielded grain sizes ranging from 100 nm to 700 nm, unprecedented in our previous investigations. Substantially improved ferroelectric and piezoelectric responses were obtained in the 800-900 °C range, with P_r values doubling to 12 $\mu A.cm^{-2}$ for films annealed at 900 °C. Moreover, the use of this additive improved leakage behavior, achieving a leakage current density of 0.1 $\mu A.cm^{-2}$ and an electrical resistivity of 10^{11} Ω.cm at 700 °C. Microscopic analyses revealed a carbon containing secondary phase at grain boundaries, probably corresponding to Li_2CO_3.

Keywords:

Aerosol deposition, thick films, post-annealing, microstructure, electrical properties

1. Introduction

For many years, piezoelectric materials have been used in a wide range of applications, mainly in the form of bulk materials. However, thinner and more adaptable materials have become increasingly necessary as technology advanced and the demand for miniaturization and precision grows. This transition from bulk to thin/thick films is particularly requested for micro-electromechanical systems (MEMS) and small-scale electronic devices. Thick films prepared from piezoelectric materials such as PZT ($PbZr_{1-x}Ti_xO_3$) and $BaTiO_3$-based compositions ($Ba_{1-x}Ca_xTi_{1-y}Zr_yO_3$, Co and Li-codoped $BaTiO_3$…) have become essential components, offering unique advantages in terms of size reduction and functional diversity. These piezoelectric thick films find their significance in applications like MEMS technology [1] sensors [2], actuators [3], transducers [4], and energy harvesters [5].

In order to prepare such films, various techniques have been explored, including sol-gel [6], screen printing [7], and inkjet printing techniques [8]. Apart from the difficult control of the thickness, the main disadvantages of these methods are the thermal treatments after deposition, devoted to the elimination of the organic components, the crystallization of the precursors and the sintering of the ceramic material. Nevertheless, the Aerosol Deposition method (AD) recently came to light due to its distinctive advantages [9]. AD process involves the generation of a dry aerosol flow from precursor ceramic powders mixed with a carrier gas (N_2, He, Ar, O_2…). These aerosol particles are then transferred into a deposition chamber, accelerated through a supersonic nozzle and directly deposited onto various substrates at

room temperature to form films / coatings. This method stands out for its ability to produce high-quality, dense, and thick films. AD allows precise control over film thickness, which is essential for MEMS and other small-scale device applications. Control of film thickness can be achieved by adjusting key parameters such as gas flow rate, deposition time, and the nature of the carrier gas [10]. However, it should be noted that the deposition efficiency of the AD process is generally low, and powder recovery systems would be necessary for industrial-scale applications to ensure material conservation. Additionally, the absence of high-temperature processing steps makes it compatible with a wide range of substrates, including heat sensitive substrates, such as metals [11], and polymers [12].

However, due to its unique deposition mechanism involving grain fracture and/or fragmentation, AD results in nano-grained film microstructure, typically with grain sizes below 50 nm [9]. The nanograined microstructure, inherent to AD films, offers certain advantages such as high dielectric strength [13,14], but also presents a substantial challenge for ferro/piezoelectric properties of the films. Indeed with such low grain sizes, AD films lose their ferro/piezoelectricity [15,16]. This phenomenon, commonly referred to as “size effect”, is a critical and well-documented factor that significantly influences the performance of such materials, and was particularly studied in the case of $BaTiO_3$ [17,18]: below a certain critical grain size, long range ferroelectric order is lost, and thus $BaTiO_3$ presents a paraelectric behavior instead of the conventional non-linear ferroelectric behavior of the bulk material. To explain the loss of ferroelectricity in nano-grained $BaTiO_3$, Hoshina et al. have proposed two mechanisms [17]. The first involves a core-shell structure, consisting of a tetragonal core and an external cubic shell. As grain size decreases, the ratio of tetragonal to cubic phases decreases, inducing the disappearance of the tetragonal core and, consequently, of ferroelectricity at grain sizes below 20-30 nm. The second mechanism is based on domain wall density. Very small grains cannot develop multi-wall ferroelectric domains. Hence, a transition from the multidomain structure to a monodomain is supposed to take place for decreasing grain size. This type of structure hinders the mobility of domains and the polarization inversion, which suppresses ferroelectric behavior.

Nevertheless, the loss of ferroelectric properties in as-deposited AD-fabricated films significantly limits their relevance for ferro / piezoelectric applications. Post-annealing treatments have been extensively explored as a way to solve this problem. Both conventional thermal annealing and non-conventional techniques have been investigated to enhance electrical properties and, specifically, to restore ferroelectricity in AD films [19–26]. The reported studies have demonstrated that post-annealing can successfully allow the recovery of ferroelectricity after annealing at different range of temperatures: ≥ 600 °C for PZT [24,27], ≥ 700 °C for KNN [23,28], ≥ 800 °C for $BaTiO_3$ [10,26,29].

However, even though electrical properties can be recovered by annealing processes, the obtained properties remain lower than those of bulk ceramics. This disparity is particularly pronounced for lead-free piezoelectric materials like $BaTiO_3$, where the electrical properties are strongly dependent of the grain size. The modest properties of annealed $BaTiO_3$ are attributed to the limited grain growth achievable within the annealing temperature ranges commonly employed, which remain several hundred degrees below the sintering temperatures of bulk $BaTiO_3$ ceramics. Indeed, most reported annealing attempts were performed at relatively low temperatures, such as 500 °C [30,31], and 750 °C [29]. Few studies have reported the use of high temperature annealing (> 1000 °C) for $BaTiO_3$ films. At such temperatures, grain growth is enhanced compared to < 1000 °C temperatures, but resulting properties still do not match those exhibited by $BaTiO_3$ ceramics [32,33]. Furthermore high-temperature annealing introduces additional complications, such as increased interfacial thermal stress between the $BaTiO_3$ layer and the substrate. This problem negatively influences

the piezoelectric properties and increases the risk of film delamination. This risk is specifically significant when considering metallic substrates, which may possess limited oxidation resistance and are thus unsuitable for high-temperature treatments, such as kovar® (Fe54/Ni29/Co17) substrates. Considering all these factors, it becomes apparent that high-temperature annealing is not the optimal strategy for enhancing the electrical properties of AD films. Instead, there is an undeniable need to investigate annealing at moderate temperatures, specifically within the 700-900 °C range. New approaches must be identified in order to promote more significant grain growth and, by extension, improve the electrical performance of $BaTiO_3$ films.

In a previous work, we successfully demonstrated that ferro/piezoelectricity could be recovered in AD-fabricated $BaTiO_3$ films through thermal post-annealing at temperatures ≥ 800 °C [10]. However, grain sizes achieved in the 800-900 °C range remained limited (≤ 100 nm). Thus, our present study introduces a new approach aiming to lower below 800 °C the annealing temperature required for restoring ferroelectricity in $BaTiO_3$ films, while also increasing the grain size compared to our previous results. For this purpose, we explored the incorporation of Li_2CO_3 into the starting $BaTiO_3$ powder. Indeed, lithium carbonate is known as one of the classical sintering aids for ceramic materials. Melting at 723°C and thus forming a liquid phase, Li_2CO_3 has already been reported to lower the sintering temperature and improve microstructural characteristics of $BaTiO_3$ based ceramics [34,35]. Currently, the use of such classical additives is so far not explored in aerosol deposited piezoelectric films.

Therefore, this study represents the first attempt of use of such a traditional sintering additive on aerosol-deposited piezoelectric films. It aims to (i) examine the initiation of grain growth by Li additive at low temperatures (< 800 °C) and hence restore ferro/piezoelectricity at such low temperatures, (ii) induce pronounced grain growth in the 800-900 °C range and thus improve the ferro/piezoelectric properties compared to “pure” $BaTiO_3$ films.

2. Experimental procedure

2.1. Powder preparation and AD process

Commercially available $BaTiO_3$ (Alfa Aesar, 99 %) and Li_2CO_3 (Sigma Aldrich, 99.99 %) powders were used for aerosol deposition (AD) of $BaTiO_3$ and $BaTiO_3$-Li_2CO_3, hereafter referred respectively as BT (d_{50} = 0.57 µm) and BT-Li (d_{50} = 0.72 µm). To obtain the BT-Li powder, 1.5 wt% of Li_2CO_3 was added to pre-treated $BaTiO_3$ powder. These two powders were mixed by ball milling for 2 hours in ethanol and then dried before being used for the deposition process.

The AD apparatus used for the deposition of prepared powders was described in our previous study [10]. The deposition process was performed using helium as a carrier gas (flow rate of 12.5 $L.min^{-1}$). The aerosol was sprayed onto the substrate (125 µm-thick kovar® foils) by a nozzle, kept at a distance of 5 mm from the substrate. The scanning speed was fixed at 1.5 $mm.s^{-1}$, allowing to deposit 5 mm x 10 mm area films. After 20 scans, the obtained thickness was in the range of 100 µm [10], and around 50 µm for the BT-Li films, highlighting the lower deposition rate of the BT-Li powder. For characterization purposes, both sets of films were adjusted to a consistent thickness of 50 µm. After deposition, films underwent thermal post-annealing in electric furnace for 3 hours under argon flux (heating and cooling of 50 $°C.h^{-1}$).

2.2. Characterization techniques

The crystal structure analysis of the elaborated films was performed using X-ray diffraction (XRD, Bruker D8 Advance X-Ray diffractometer in Bragg-Brentano geometry, 2θ range 20° - 80°, Cu Kα radiation). The determination of crystallite size and microstrain was based on the Full Width at Half Maximum (FWHM) of the XRD peaks by means of the Williamson-Hall

method. Raman spectroscopy was used to investigate the local structure of the BT films, as well as to assess internal stress (T64000 HORIBA Jobin–Yvon spectrometer, triple subtractive configuration, 200–900 cm^{-1} range, 532 nm wavelength). Baseline correction (linear correction) and normalization (total area normalization) procedures were applied to the obtained Raman spectra. Elemental analysis and cross-section observations were performed using scanning electron microscopy (Zeiss Crossbeam 550 SEM), with Focused Ion Beam (FIB) and Energy-dispersive X-ray spectroscopy (EDS). Additionally, high-resolution transmission electron microscopy (TEM) and scanning transmission electron microscopy (STEM) analysis was carried out (JEOL JEM 2100F) to validate the microstructural differences derived from XRD data and SEM surface observations. SEM and TEM/STEM images were treated using ImageJ software, in order to quantify porosity ratio and grain size distribution of the films [36].

Electrical characterizations of the BT and BT-Li films were performed using a ferroelectric analyzer (TF 2000, aixACCT Systems GmbH). Before measurements, silver electrodes were deposited onto the top surface of the examined samples, followed by poling under 5 $kV.mm^{-1}$ for 30 min at room temperature. Polarization-Electric field (P-E) and Strain-Electric field (S-E) loops were measured at 10 Hz using a 10 $kV.mm^{-1}$ triangular waveform signal. Leakage current density (j-E) measurements were performed using a 10 $kV.mm^{-1}$ DC electric field, incrementing in 0.5 $kV.mm^{-1}$ steps with a dwell time of 2 s at each step.

3. Results and discussion

3.1. Structural analysis

Figure 1 shows the XRD patterns of BT and BT-Li films annealed at 650, 700, 800, and 900 °C. Due to the susceptibility of kovar® sheets to oxidation, peaks associated with Fe, Ni and Co oxides (PDF #66-0246 for $Co_{0,5}Ni_{0,5}Fe_2O_4$, and #71-0073 for α-Fe_2O_3) are observed for all annealing temperatures, although annealing was carried out under an argon flux. However, this oxidation is less pronounced compared to our previous studies involving BT films deposited on kovar® and annealed in air atmosphere [10].

Furthermore, the main peaks of the XRD patterns correspond to the $BaTiO_3$ perovskite phase (PDF #05-0626). Except for the 900 °C annealed BT-Li film, the peak positions are shifted toward lower diffraction angles upon Li addition. This observation suggests a modification of the mean lattice parameters for BT-Li films compared to BT ones. However, the peak splitting, indicative of tetragonal symmetry, was not identified in the XRD patterns. Indeed, the broadening of the XRD peaks, attributed to the reduced crystallite sizes in AD- films, does not allow to separate splitted peaks, like (200) and (002), or (202) and (220). Finally, compared to BT films, the BT-Li films exhibit enhanced peak intensities and narrower peak widths for all annealing temperatures. This result is clearly associated with an improvement of crystallinity, suggesting that Li incorporation facilitates grain growth during annealing. Interestingly, the most marked enhancement in peak intensity is noted for samples annealed at low temperatures (650 and 700 °C).

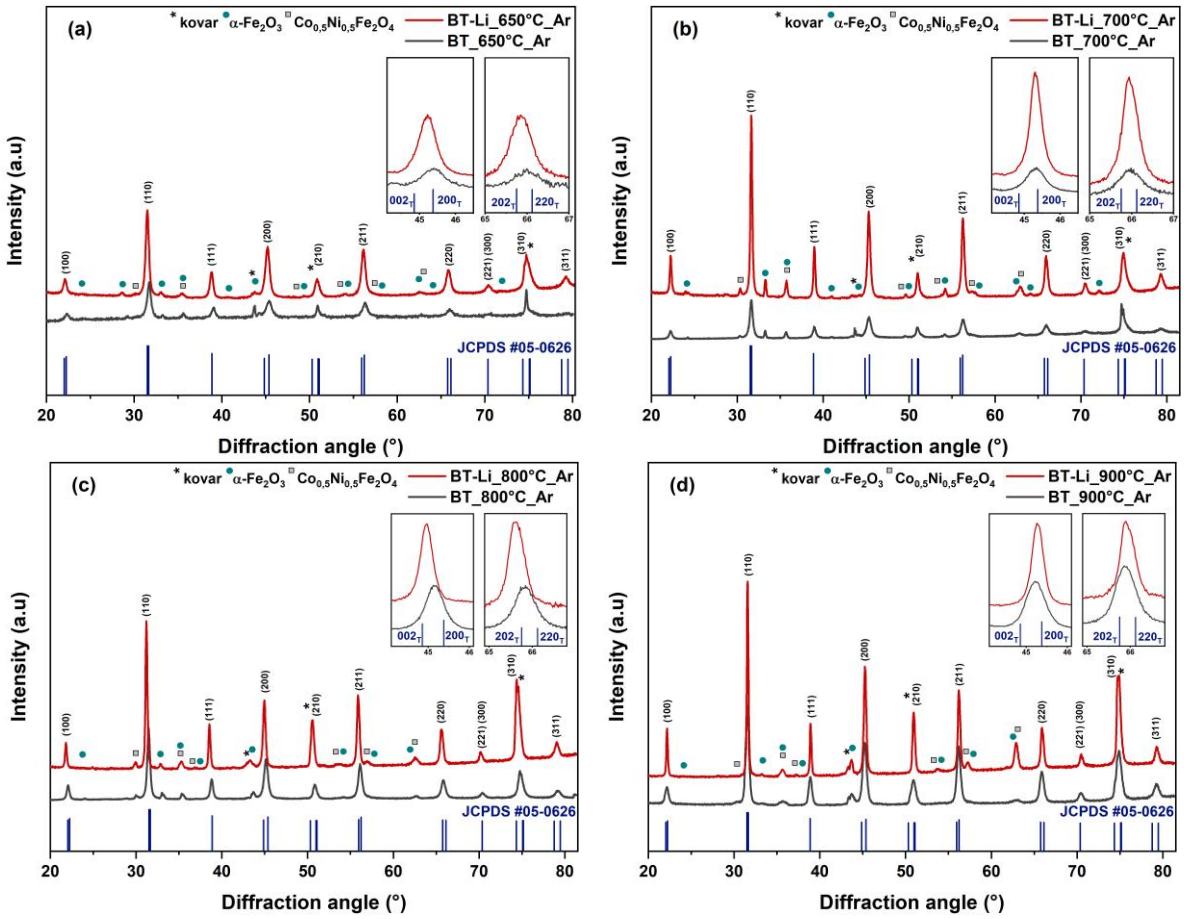

Figure 1: XRD patterns of BT and BT-Li films annealed at (a) 650 °C, (b) 700 °C, (c) 800 °C, and (d) 900 °C (the peak indexing in the upper part of the figure corresponds to pseudo-cubic symmetry, JCPDS card is for $BaTiO_3$ tetragonal symmetry) (two-column, color online)

In addition, a quantitative evaluation of the influence of the Li additive on crystallinity was performed using the Williamson-Hall method. This approach allows the separation of crystallite size and microstrain contributions to XRD peak broadening [37,38]. The resulting data are detailed in Table 1 (see supplementary materials for detailed plot). In the absence of Li, crystalline growth in BT films is only evident at temperatures above 800 °C. The results also reveal a modest effect of the Li additive on crystallite size at 650 °C. Indeed, BT-Li film shows only slightly higher crystallite size compared to BT film, both remaining in the 25-30 nm range. With increasing annealing temperature, more evident differences in crystallite sizes emerges between BT and BT-Li films. At 700 °C, significant crystal growth is observed exclusively in the BT-Li film, with a crystallite size approaching 80 nm, compared to 24 nm for BT film. For the 800 °C annealed samples, BT-Li films exhibit a remarkable increase in crystallite size. A similar trend is observed at 900 °C, with the BT-Li films presenting a crystallite size 5.6 time larger than the one of the as-deposited film, while the increase factor is only 2.6 for BT film. As reported in our previous study, argon annealing also induces a reduction of microstrain compared to the as-deposited films, with a similar trend for both BT and BT-Li films.

Collectively, these results demonstrate the efficiency of Li additive in promoting grain growth, which is evident at temperatures as low as 650 and 700 °C, and increases by over 100 % in the 800-900 °C temperature range. Additionally, a general trend of increasing crystallite size with rising annealing temperature is confirmed for both BT and BT-Li samples. Consequently, the largest crystallite size of approximately 143 nm is obtained for the 900 °C annealed BT-Li film.

Table 1: Crystallite size and microstrain values obtained for BT and BT-Li films using Williamson-Hall method (one-column)

Film	Annealing temperature (°C)	Crystallite size (nm)	Microstrain (%)
BT	As deposited	26.2 ± 2.5	0.55 ± 0.11
BT-Li		25.6 ± 2.3	0.54 ± 0.12
BT	650	25.3 ± 1.9	0.20 ± 0.03
BT-Li		29.7 ± 1.7	0.21 ± 0.03
BT	700	24.2 ± 2.0	0.12 ± 0.04
BT-Li		76.2 ± 1.0	0.15 ± 0.02
BT	800	36.3 ± 0.9	0.10 ± 0.02
BT-Li		83.2 ± 0.6	0.07 ± 0.02
BT	900	68.0 ± 0.7	0.13 ± 0.01
BT-Li		143.5 ± 0.4	0.11 ± 0.01

Figure 2a presents the Raman spectra of the annealed BT and BT-Li films. Two Raman bands typical of the tetragonal phase are observed at 305 cm^{-1} (E(LO + TO), B_1) and 720 cm^{-1} (E(LO), A_1(LO)) for all the samples [39,40]. Therefore, all spectra are attributable to the tetragonal phase of $BaTiO_3$. Notably, these bands exhibit increased intensity in the case of BT-Li films, particularly for the 720 cm^{-1} band (Fig. 2c). This latter observation can be related to enhanced grain growth for BT-Li films and hence to increased tetragonality, since tetragonality is closely linked to grain size within the examined grain size range [18].

Furthermore, the 515 cm^{-1} band, typically shifted to higher wavenumbers with increasing internal stress in $BaTiO_3$, tends to shift back towards lower wavenumbers in Li-incorporated films, particularly for the samples annealed at 800 and 900 °C (Fig. 2b) [41]. This shift indicates a decrease in macroscopic in-plane stress, which is primarily due to substrate constraints, in these BT-Li films.

In summary, Raman spectroscopy provides two key insights: (1) the increased intensity of the 720 cm^{-1} band supports the observation of enhanced crystallinity in BT-Li films, and (2) the shift of the 515 cm^{-1} band suggests a relative decrease in macroscopic internal stress in BT-Li films compared to BT films, corroborating the XRD Williamson-Hall results.

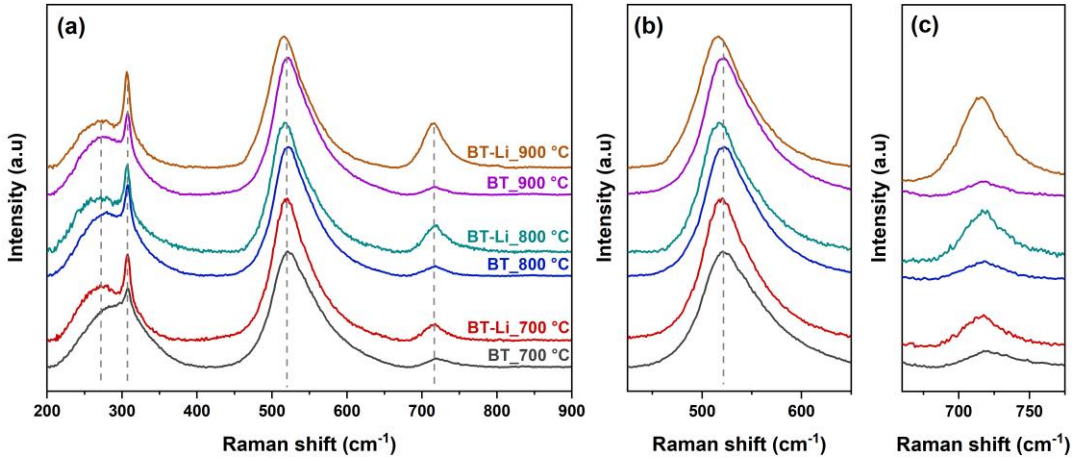

Figure 2: (a) Raman spectra of annealed BT and BT-Li films, zoom on (b) 515 cm^{-1} and (c) 720 cm^{-1} bands (two-column, color online)

3.2. Microstructural observations

Top surface SEM images for BT and BT-Li films annealed at 700 °C, 800 °C, and 900 °C are presented in figure 3. These micrographs display clear differences in morphology between the BT and BT-Li films for all annealing temperatures. For BT films, the surface morphology appears relatively smooth and partly conserves the crater-like features observed for the as-deposited films. Notably, SEM images reveal almost no distinct grains on the top surface of the BT films, with only few grains observed for the 900 °C annealed BT film.

In contrast, the BT-Li films exhibit a clearly rougher surface texture. At 700 °C, a significant decrease in the cratered surface occurs to completely disappear at 800 °C and 900 °C. Moreover, small and distinct grains are evidenced, suggesting grain growth in the BT-Li samples for all examined temperatures. Specifically, for the 700 °C annealed BT-Li film, grain growth appears to be incomplete, with smooth, grain-free regions still present. At 800 °C, grain growth progresses to cover the entire surface. This trend continues at 900 °C, with visibly larger grains. Estimations from the SEM images suggest grain sizes of approximately 50-100 nm for the 700 °C annealed BT-Li film, 50-150 nm for the 800 °C annealed film and finally 100 to 250 nm for those annealed at 900 °C.

These microstructural observations are consistent with the XRD and Raman results, confirming an enhanced crystallinity promoted by Li additive. Indeed, grain growth is initiated at temperatures as low as 700 °C with the introduction of Li. Moreover, a clear trend of increasing grain size is observed with higher annealing temperatures (800-900 °C). Finally, the size of the observed surface grains is consistent with the crystallite sizes previously determined by the Williamson-Hall method.

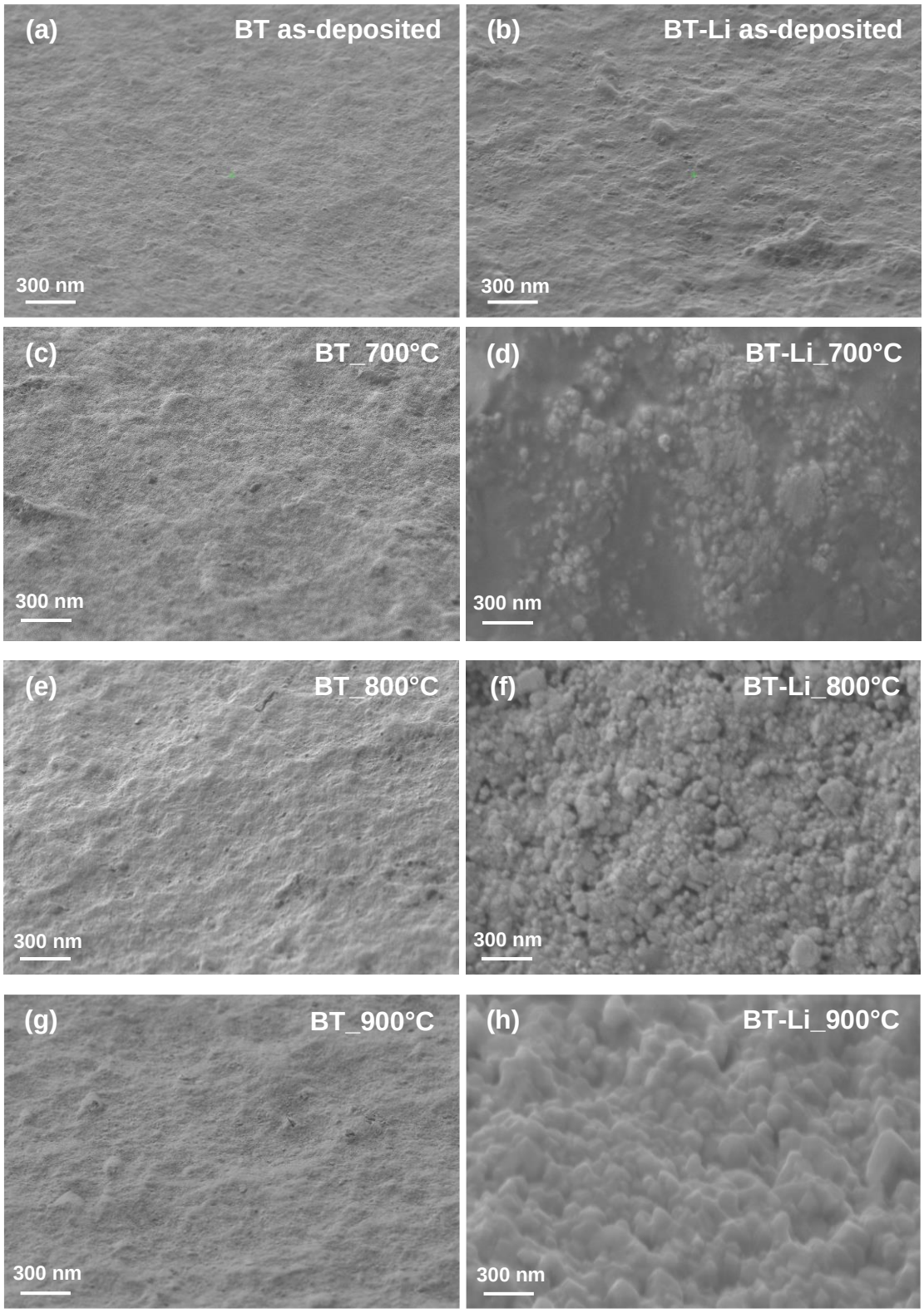

Figure 3: Top surface SEM images of as-deposited (a) BT and BT-Li films, 700 °C annealed (c) BT and (d) BT-Li film, 800 °C annealed (e) BT and (f) BT-Li film, and 900 °C annealed (g) BT and (h) BT-Li film (two-column, color online)

Figure 4 shows cross-section SEM images of as-deposited BT and BT-Li films. The BT film (Fig. 4a) presents a highly dense microstructure with only few stacking defects. Quantification of porosity ratio using imageJ treatment revealed low values, typically less than 1 %. In contrast, the BT-Li film (Fig. 4b) exhibits a notably porous microstructure, characterized by the

presence of lamellar-shaped pores. The porosity ratio for the BT-Li film, as determined via ImageJ analysis of the cross-section SEM images, is approximately 8.4 %.

The observed high density of BT films contrasts sharply with the porous nature of the as-deposited BT-Li films. This discrepancy is attributed to the formation of agglomerated particles due to the incorporation of Li_2CO_3 into the starting BT powder. The hygroscopic nature of Li_2CO_3 likely led to the absorption of ambient moisture during the powder preparation process, thus inducing agglomeration. Indeed, previous studies have shown that powders exhibiting significant agglomeration are prone to yield films with increased porosity when deposited by AD [42].

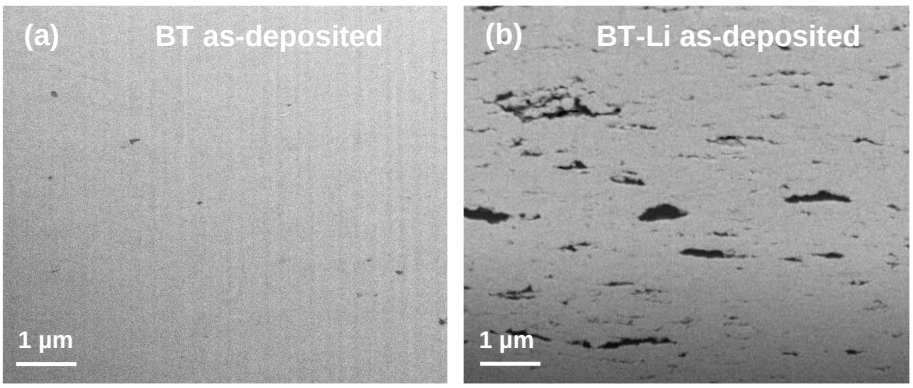

Figure 4: Cross-sectional images of as-deposited (a) BT and (b) BT-Li films (two-column, color online)

Despite the initial porosity observed in the BT-films, annealing leads to microstructural evolution shown in Figure 5. For the lowest annealing temperature of 650 °C (Fig. 5a), the pore distribution becomes more homogeneous compared to the as-deposited sample (Fig. 4b). Furthermore, the pore size decreases, leading to a slight reduction of the porosity ratio to 7.4 %.

For 700 °C, the homogenization of the microstructure continues and the average pore size decrease (Fig. 5b), following a trend similar to that observed at 650 °C, although some large lamellar pores are still present. A more pronounced transformation occurs at 800 °C (Fig. 5c), where both the number and size of the pores decrease significantly. The shape of these pores suggests partial closure during annealing, and the transition from lamellar to more spherical shapes. Hence, the porosity ratio for this sample decreases to 4.1 %. The densification process continues in the BT-Li film annealed at 900 °C (Fig. 5d), for which porosity ratio significantly decreases to an estimated value of 1.2 %.

Globally, the decrease in porosity ratio observed after annealing very likely indicates a sintering process promoted by the Li additive. Despite initially increasing porosity in the as-deposited films (8.4 %), the Li additive effectively consolidates the microstructure. It also significantly reduces porosity with increasing temperatures, leading to a low porosity ratio of 1.2 % at 900 °C. On the other hand, in the cross-sections of the annealed BT-Li films, small areas exhibiting distinct chemical contrast were identified (see green square in Fig. 5d). This suggests the occurrence of a Li-rich phase that remains in the microstructure after annealing in the 600-900 °C temperature range. The chemical composition and the effect of this secondary phase will be discussed hereafter.

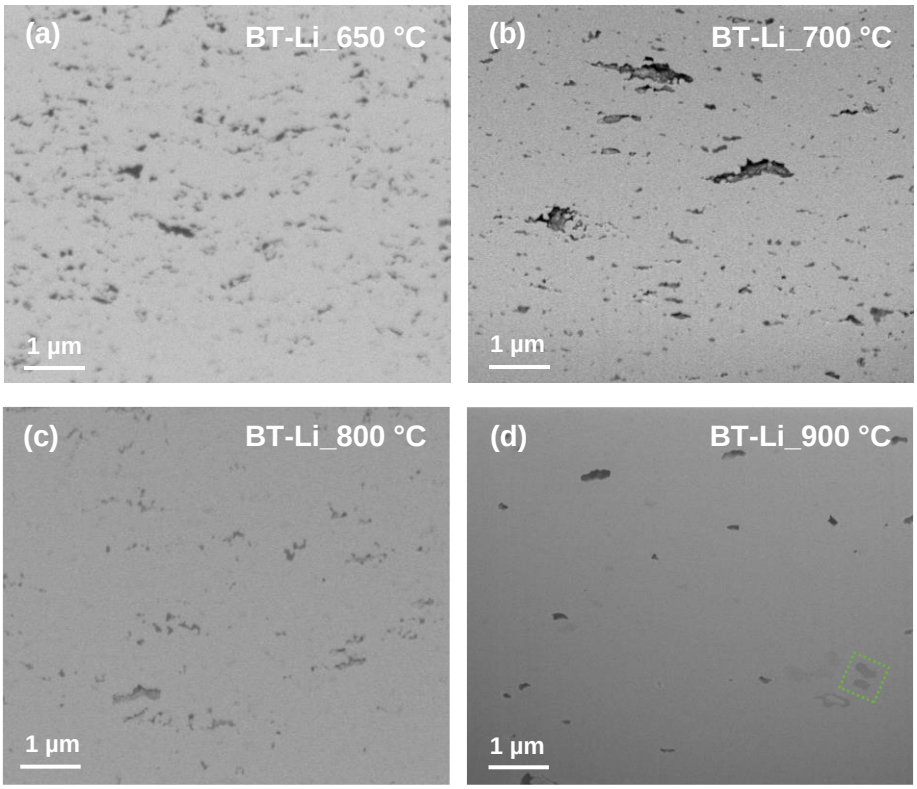

Figure 5: Cross-section images of BT-Li films after thermal annealing at (a) 650 °C, (b) 700 °C, (c) 800 °C and (d) 900 °C). The dashed green square in (d) highlights a region where a Li-rich phase was identified. (two-column, Color online

The microstructural and grain size changes induced by the Li additive in the BT-Li films were evaluated more precisely using TEM and DF-STEM (Dark Field-Scanning Transmission Electron Microscopy). The microstructure of the 700 °C annealed BT-Li film (Fig. 6a) evidence faceted and consolidated grains. Their size varies from very fine grains (10-30 nm) to significantly larger grains exceeding 100 nm. Such grains with a size exceeding 100 nm were not observed in previous work for BT films, even for an annealing temperature of 900 °C [10].

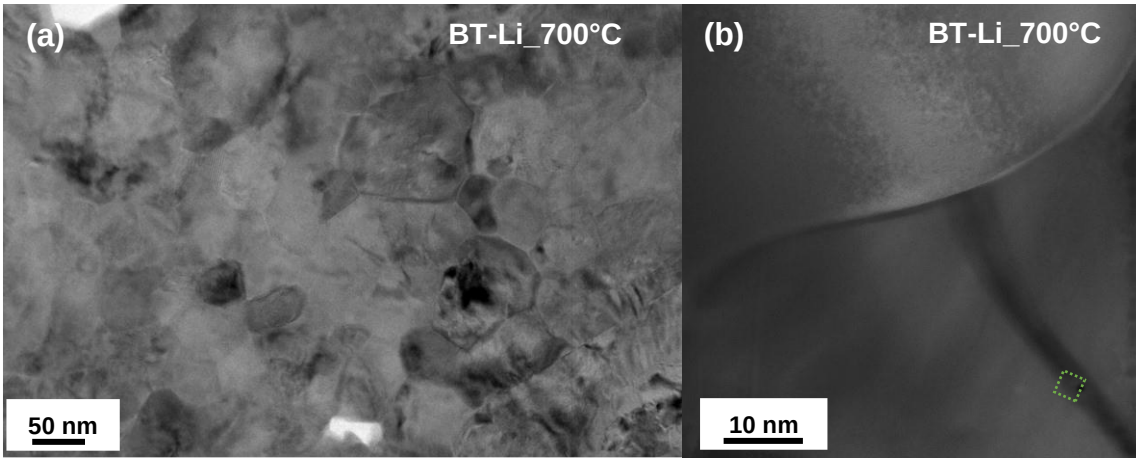

Figure 6: (a) TEM and (b) Dark-Field STEM images of 700 °C annealed BT-Li film. The dashed green box in (b) highlights the secondary Li-rich phase analyzed by EDS. (two-column, color online)

For the BT-Li film annealed at 800 °C, faceted and consolidated grains are also observed (Fig. 7a). These grains are notably larger (50-150 nm) than those obtained for the 700 °C annealed sample, confirming a more pronounced grain growth.

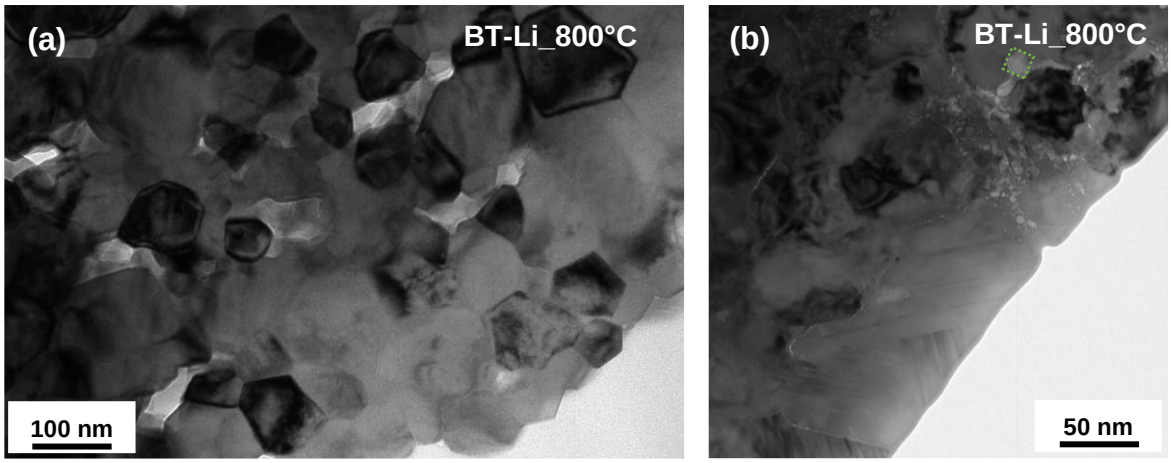

Figure 7: TEM images of 800 °C annealed BT-Li film. The dashed green box in (b) highlights the secondary Li-rich phase analyzed by EDS. (two-column, color online)

For the BT-Li film annealed at 900 °C, BF STEM image reveals a very dense microstructure with a considerable variation in grain size (Fig. 8a), ranging from approximately 100 nm to significantly larger sizes of 500-700 nm.

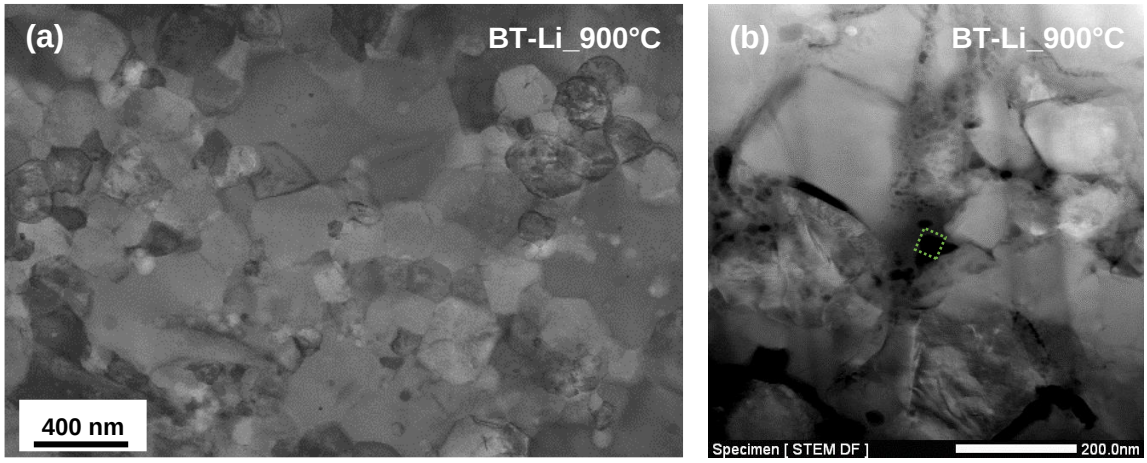

Figure 8: (a) Bright-Field and (b) Dark-Field STEM images of 900 °C annealed BT-Li film. The dashed green box in (b) highlights the secondary Li-rich phase analyzed by EDS. (two-column, color online)

In order to quantify the observed evolution, Image J analysis was also performed on the 700, 800, and 900 °C BT-Li films (Fig. 9). For 700 °C, the calculation of a grain size distribution (Fig. 9a) reveals a high concentration of grains in the 30-70 nm range, with an estimated mean size of 56 nm and a standard deviation of 16 nm, suggesting a relative uniformity in grain size. For 800 °C (Fig. 9b), the analysis identified grains mainly between 40 and 150 nm. The average grain size has increased to 82.5 nm with a standard deviation of 26.7 nm, confirming grain growth. At 900 °C, the distribution is broader (Fig. 9c) compared to the 700 and 800 °C annealed films, with mainly grains surpassing 100 nm. Interestingly, $BaTiO_3$ grains exceeding 200 nm were observed for the first time, with an average diameter of 210 nm, accompanied by a substantial standard deviation of 101 nm, confirming a broad grain size distribution. These observations corroborate previous top surface SEM findings, demonstrating a consistent trend of grain growth in annealed BT-Li films, in agreement with XRD results.

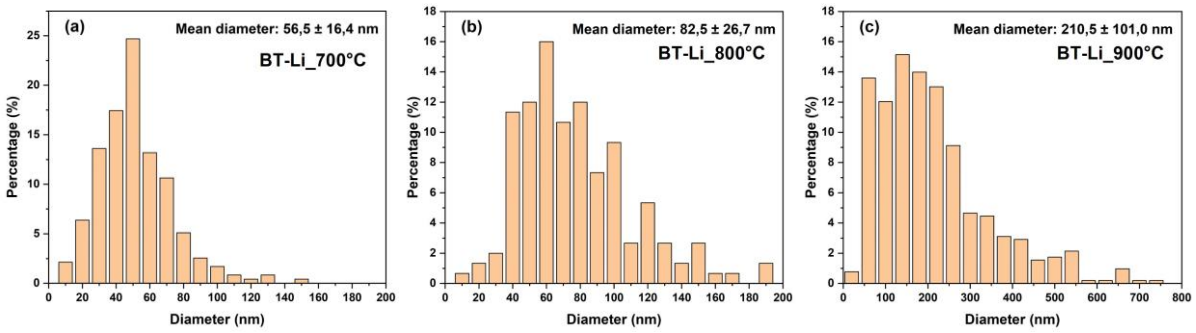

Figure 9: Grain size distribution calculated using ImageJ for (a) 700 °C, (b) 800 °C and (c) 900 °C annealed BT-Li film (one-column, color online)

Furthermore, a secondary phase, distinct from $BaTiO_3$, was also observed at the grain boundaries (Fig. 6b, 7b and 8b, green dots squares). Local EDS analysis performed on this secondary phase identified the presence of carbon (C), along with Ba, Ti, and O (Fig. 10). Since the EDS analysis has limited spatial resolution and thus includes both grains and grain boundaries, the detected Ba and Ti probably comes from $BaTiO_3$ grains. The carbon content suggests a potential secondary phase, consistent with carbon occurrence induced by the Li_2CO_3 additive. The elemental percentages obtained are used only for relative comparisons, since heavier elements (here Ba and Ti) are more easily detected than lighter ones (C and O), perhaps leading to underestimation of concentration for the latter elements. At 800 °C, the carbon content appears as lower than for the 700 °C annealed film and this decrease continues for the 900 °C annealing temperature. It is noteworthy that the observation of the secondary phase does not concern all the observed sample areas, as it does not seem to be homogeneously present within the annealed samples. However, this secondary phase at grain boundaries probably comes from the Li additive. A more detailed discussion of the decomposition of the Li_2CO_3 additive, its interaction with the $BaTiO_3$ matrix, and the formation of the secondary phase at grain boundaries will be provided in the last section.

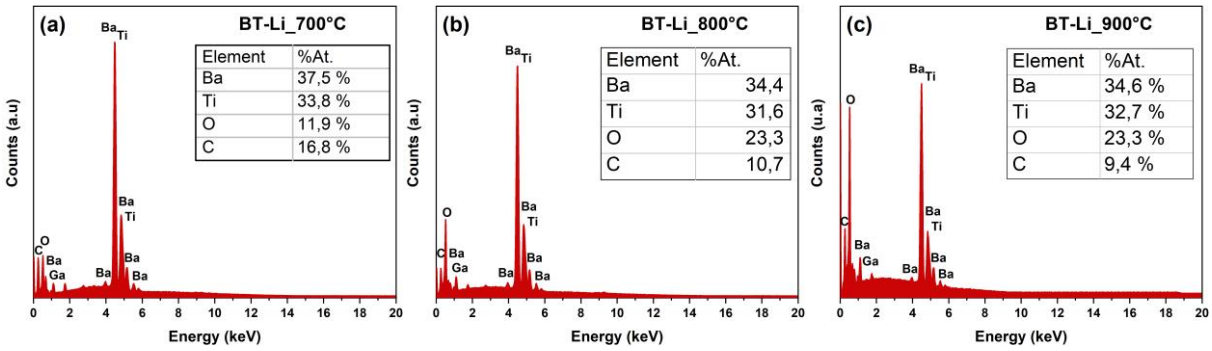

Figure 10: EDS analysis performed on the secondary phase observed for the (a) 700 °C, (b) 800 °C and (c) 900 °C annealed BT-Li film (one-column, color online)

3.3. Electrical properties

The polarization-electric field (P-E) loops measured for annealed BT and BT-Li films are presented in figure 11. P-E loops measured for the film annealed at 650 °C (Fig. 11a) reveal marked differences in ferroelectric behavior between BT and BT-Li films. The BT film displays a linear, non-ferroelectric behavior, whereas the BT-Li film exhibits distinct non-linear ferroelectric P-E loop, evidencing the recovering of ferroelectricity by annealing. The BT-Li film (Fig. 11a) presents a maximum polarization (P_{max}) of 9.5 $\mu C.cm^{-2}$, substantially exceeding the value of 3.1 $\mu C.cm^{-2}$ measured for the BT film. For the annealing temperature of 700 °C (Fig. 11b), the BT film maintains a linear P-E loop indicative of non-ferroelectric behavior, while the

BT-Li film demonstrates again a distinctly non-linear ferroelectric P-E loop. The BT-Li film shows an increased P_{max} value of 11.4 µC.cm^{-2}, compared to 6.1 µC.cm^{-2} for the BT film.

At 800 °C (Fig. 11c), both BT and BT-Li films exhibit non-linear ferroelectric P-E loops, but their shapes reveal different ferroelectric behavior. The BT film P-E loop display weak non-linearity, while for the BT-Li film, a well-defined hysteresis loop with reduced leakage and a lower coercive field (E_c) is observed, indicating enhanced ferroelectricity. Despite its weaker hysteresis, the BT film presents higher P_{max} and P_r values, potentially due to leakage contributions at high electric field. This divergence in behavior extends to the 900 °C annealed samples (Fig. 11d), where the BT-Li film P-E loop is sharply defined. The latter also presents a significant increase in both P_{max} and P_r values, alongside a decrease in E_c. Specifically, the P_r value for the BT-Li film doubles from 6.6 µC.cm^{-2} for the BT film to approximately 12.0 µC.cm^{-2}.

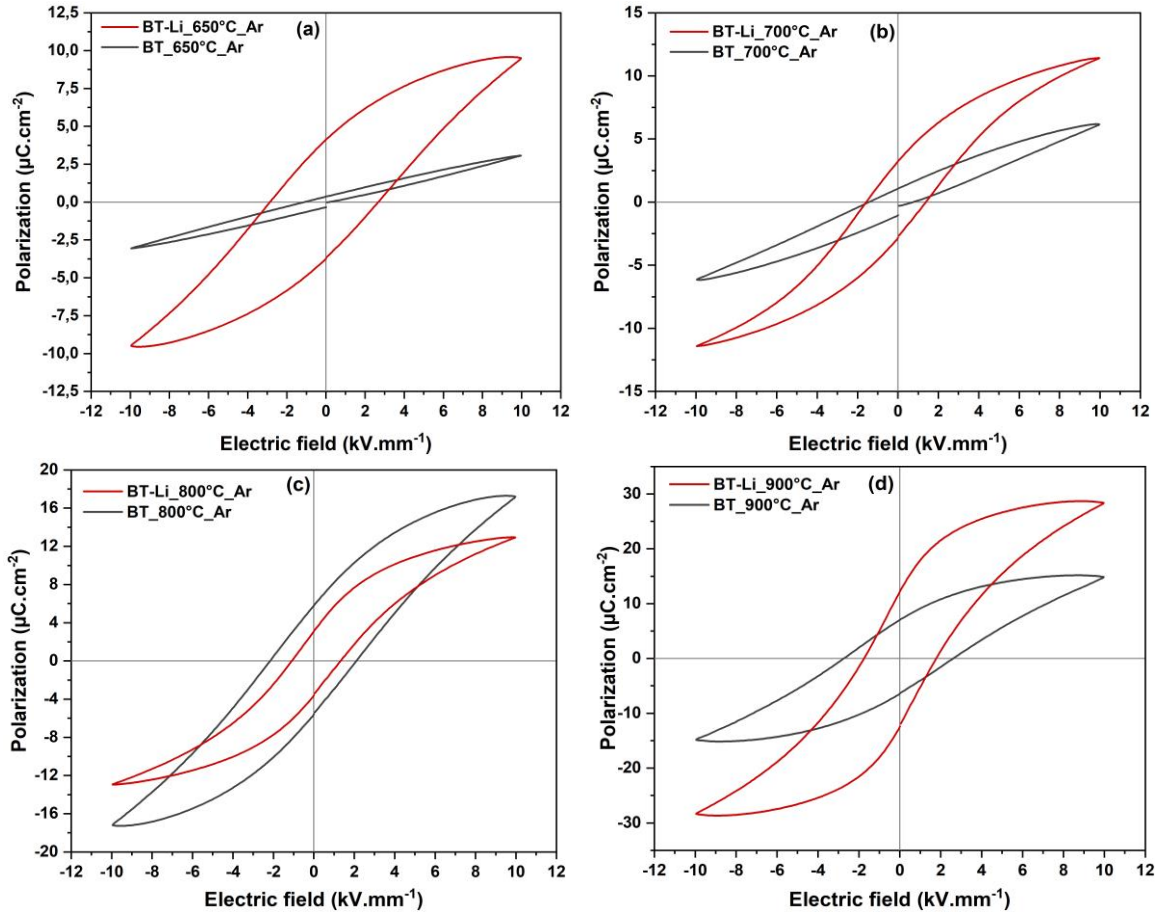

Figure 11: Polarization-Electric field (P-E) loops measured for (a) 650 °C, (b) 700 °C, (c) 800 °C and (d) 900 °C annealed BT and BT-Li films (two-column, color online)

Figure 12 presents the strain-electric field (S-E) butterfly loops, corresponding to the P-E loops of figure 11. It is important to note that these strain measurements could potentially be influenced by layer bending due to the d_{31} transverse mode and therefore are mainly considered for comparative purposes of the different samples. At 650 °C (Fig. 12a), BT-Li film exhibits a piezoelectric strain response to the applied electric field, ranging from 0.04 to 0.06 % under 10 kV.mm^{-1}, confirming the successful recovery of ferro/piezoelectricity at this low temperature. In contrast, the BT film annealed at the same temperature exhibits only a low amplitude, irregular strain response, underscoring the lack of piezoelectricity; in agreement with the P-E loop. For the 700 °C annealed films (Fig. 12b), the S-E curves reveal a significant strain response for the BT-Li film (0.04 %), confirming the recovery of piezoelectricity. On the

other hand, the BT film presents a negligible and irregular strain response, still in agreement with the corresponding P-E loop.

At 800 °C (Fig. 12c), both BT and BT-Li films exhibit quite comparable butterfly loop strain responses, each presenting a maximum strain of approximately 0.02-0.03 % for an applied electric field of 10 kV.mm^{-1}. However, for 900 °C (Fig. 12d), a notable divergence in piezoelectric strain response is observed, due to the incorporation of the Li additive. The BT-Li film annealed at this temperature exhibits a strongly enhanced strain response, estimated between 0.07 and 0.09 %, which is considerably larger than the 0.04 % strain observed for the BT film. This disparity highlights the pivotal role of the Li additive in amplifying the piezoelectric response of BT-Li films at moderately high temperatures.

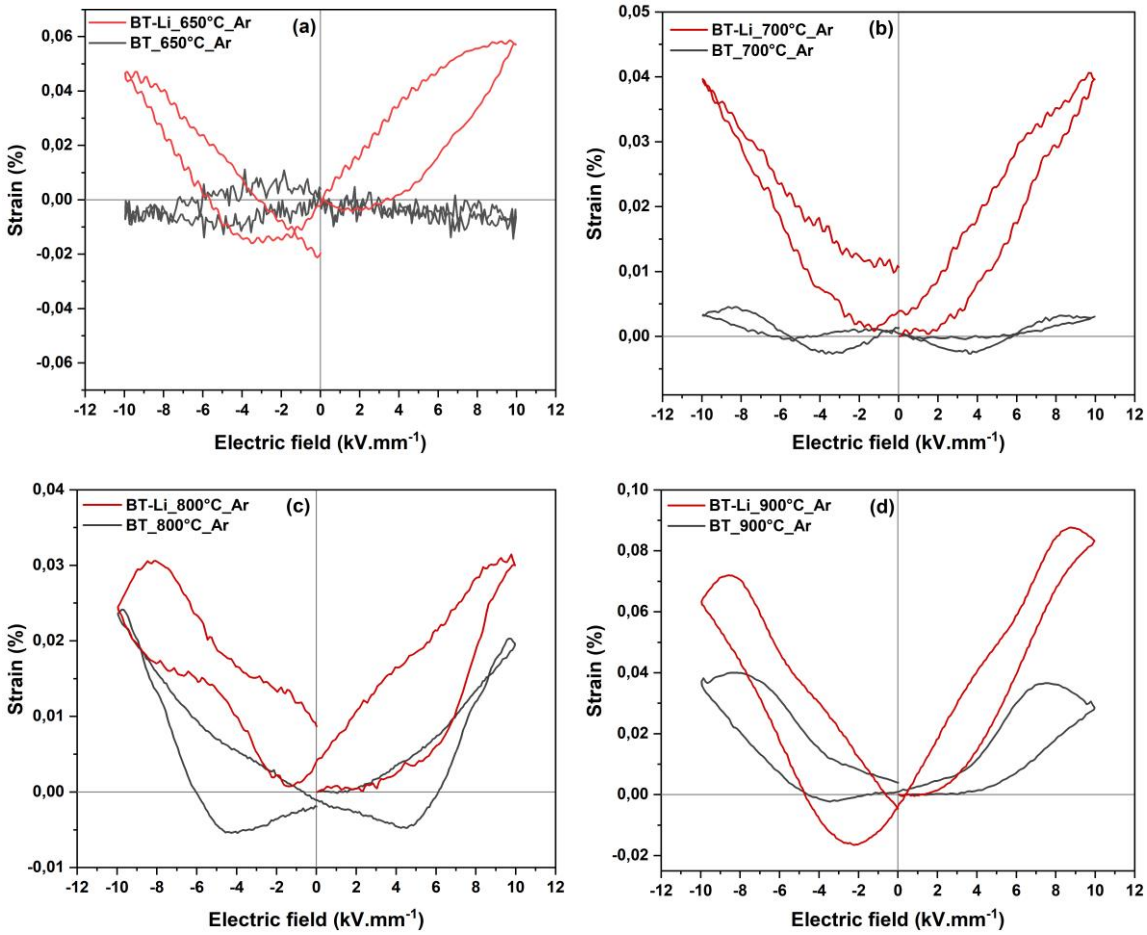

Figure 12: Strain-Electric field butterfly loops measured for (a) 650 °C, (b) 700 °C, (c) 800 °C and (d) 900 °C annealed BT and BT-Li films (two-column, color online)

The analysis of P-E and S-E loops decisively highlights the profound impact of microstructural changes induced by Li_2CO_3 addition, on the ferro/piezoelectric behavior of the films. The notable improvement in ferroelectric properties, evidenced by well-defined P-E loops with increased P_r and lower E_c, is attributed to the growth of larger grains in the presence of Li additive. Given the correlation between grain size and ferroelectric domain size [43], the promotion of grain growth by Li additive leads to larger ferroelectric domains. This facilitates the realignment of ferroelectric domains under electric field, thus lowers E_c and enhances polarization values. However, the large P_r value of 12 µC.cm^{-2} measured for the 900 °C annealed BT-Li film cannot be attributed only to grain growth, considering the limited grain size range not reaching the 1-2 µm range, typically considered optimal for $BaTiO_3$ [44]. Hence, other factors such as tensile stress generated during heat treatment probably also contributes to the

enhancement of the ferroelectric response, as discussed in our previous study on 900 °C annealed BT films [10].

The leakage current density curves (j-E) for BT and BT-Li annealed films are represented in figure 13. For the films annealed at 650 and 700 °C (Fig. 13a and 13b), similar observations can be drawn from the j-E results. For both temperatures, the BT-Li films demonstrate a notable improvement in leakage behavior. Specifically, at 700 °C, the BT-Li film exhibits a significant reduction in maximum leakage current density to about 0.1 $\mu A.cm^{-2}$ for an electric field of 10 $kV.mm^{-1}$, significantly lower by a factor 15 compared to the BT film (1.8 $\mu A.cm^{-2}$). This improvement is also reflected by an increase in the electrical resistivity for the BT-Li films annealed at 650 and 700 °C to approximately 10^{11} Ω.cm, in contrast to 10^{10} Ω.cm observed for the BT films.

For films annealed at 800 °C (Fig. 13c), the BT-Li film continues to show a significant decrease in leakage current density compared to the BT film. The latter exhibits a leakage current density of 3.4 $\mu A.cm^{-2}$ under a 10 $kV.mm^{-1}$ electric field, while the BT-Li film displays a reduced density of approximately 1.2 $\mu A.cm^{-2}$. This reduction in leakage current is mirrored by an increase in electrical resistivity from 10^{9} Ω.cm for the BT film to 10^{11} Ω.cm for the BT-Li film. Upon annealing at 900 °C (Fig. 13d), an overall increase in leakage currents is observed in both films, as expected at higher temperatures. However, the BT-Li film consistently shows a reduced leakage current compared to the BT film, maintaining the observed trend. Under 10 $kV.mm^{-1}$, the BT-Li film presents a lower current density (3.9 $\mu A.cm^{-2}$) than the BT film (10.1 $\mu A.cm^{-2}$), correlated to a higher electrical resistivity of 2×10^{10} Ω.cm for the BT-Li film, compared to 7×10^{9} Ω.cm for the BT film.

These results corroborate the previous discussions regarding the microstructural enhancements brought about by the Li additive. The decreased leakage current density and increased electrical resistivity in the BT-Li films can be attributed to grain growth promoted by the Li additive. Larger grains tend to decrease the number of grain boundaries and defects, thereby reducing leakage currents and enhancing the overall electrical resistivity of the samples.

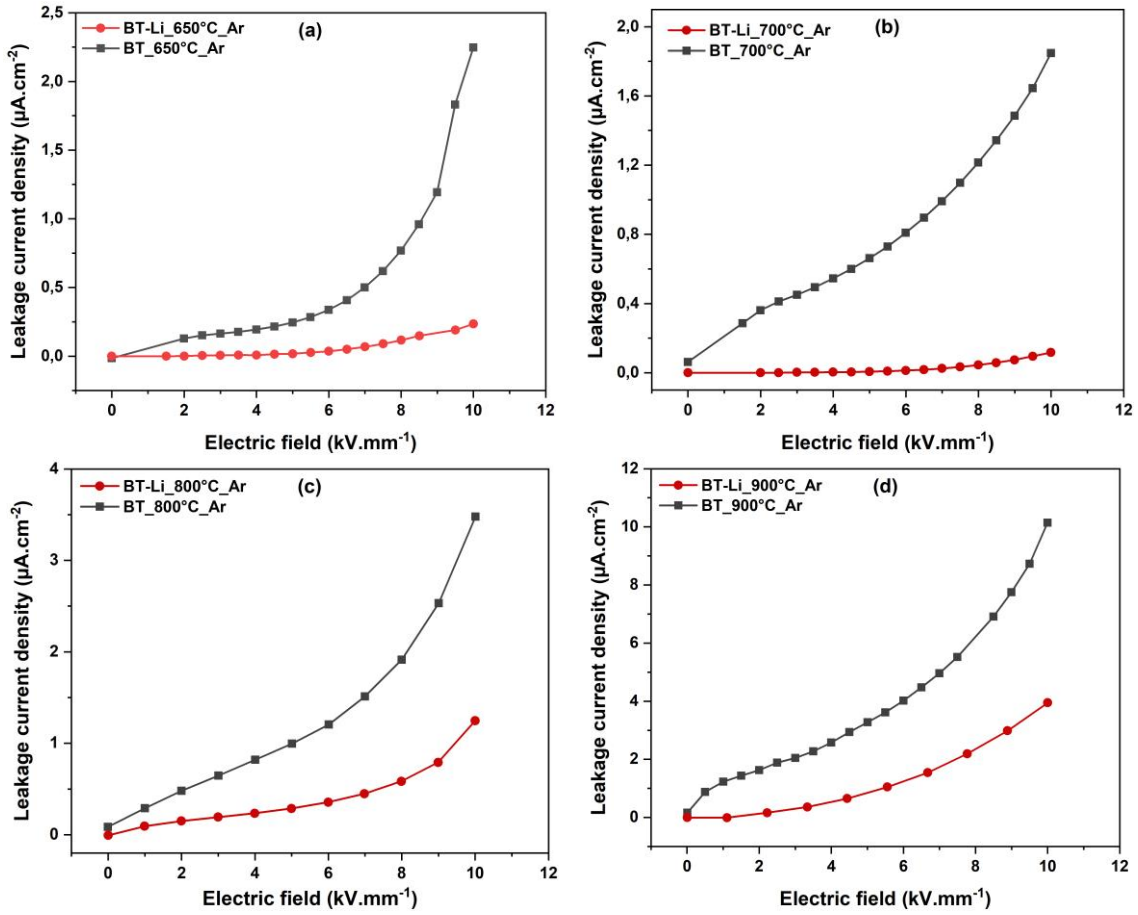

Figure 13: Leakage current density vs. Electric field (j-E) curves measured for (a) 650 °C, (b) 700 °C, (c) 800 °C and (d) 900 °C annealed BT and BT-Li films (two-column, color online)

3.4. Mechanism of action of the Li additive

The presented characterizations highlight that the incorporation of the Li additive significantly improves ferro/piezoelectric properties and reduces leakage in BT-based films. However, it is essential to elucidate the mechanism by which the Li additive influences BT-Li films during the annealing process. The incorporation of the Li additive within the BT powder may lead to two plausible mechanisms, as dopant or as fluxing agent.

3.4.1. Li as a dopant:

In this scenario, Li may potentially substitute for Ba or Ti in the $BaTiO_3$ matrix. In such a case, it would act as a p-type dopant (acceptor), leading to the creation of additional oxygen vacancies. The following reactions summarize the two possible substitution reactions:

$$2BaTiO_3 + Li_2CO_3 \rightarrow 2Ba_{Ba}^{x} + 2Li_{Ti}^{'''} + 3O_O^x + 3V_O^{\bullet\bullet} + 2TiO_2 + CO_2(g) \quad \text{(Eq. 1)}$$

$$2BaTiO_3 + Li_2CO_3 \rightarrow 2Li_{Ba}^{'} + 2Ti_{Ti}^{x} + 5O_O^x + V_O^{\bullet\bullet} + 2BaO + CO_2(g) \quad \text{(Eq. 2)}$$

Considering these reactions, such substitutions would introduce more oxygen vacancies in addition to those formed during the deposition process. While oxygen vacancies may play a role in diffusion processes, it is primarily the diffusion of cations, which occurs more slowly, that controls grain growth. Therefore, the influence of oxygen vacancies on grain growth is likely limited. Moreover, the increase in oxygen vacancies could potentially lead to higher leakage currents, complicating the poling process of the samples. This observation, however, contradicts the behavior seen in the BT-Li films.

Furthermore, the substitution of Ba^{2+} or Ti^{4+} by Li^{+} is unlikely, because of the significant difference in ionic radii between Li^{+} and the host cations Ba^{2+} and Ti^{4+}, as well as the resulting impact on the Goldschmidt tolerance factor. For $BaTiO_3$, where Ba^{2+} occupies the A-site (twelvefold coordination) and Ti^{4+} occupies the B-site (sixfold coordination), the tolerance factor is approximately 1.06, indicating a stable perovskite structure. If Li^{+} (0.76 Å for sixfold coordination) were to substitute Ba^{2+} (1.61 Å for twelvefold coordination), the tolerance factor would decrease to 0.85, leading to a destabilized structure. Similarly, if Li^{+} were to substitute Ti^{4+} (0.605 Å for sixfold coordination) at the B-site, the tolerance factor would increase to approximately 1.22, which is also outside the stable range for perovskites (typically between 0.8 and 1.1).

Moreover, since Li^{+} has lower polarizability compared to Ba^{2+}, this substitution would theoretically result in a reduction of polarization values for BT-Li films. However, our results reveal the opposite trend, with both P_{max} and P_r increasing in BT-Li films. Additionally, acceptor dopants are known to induce ferroelectric hardening in piezoceramics, making them more resistant to polarization reversal [45]. This effect, often associated with creation oxygen vacancies, was not observed here, since a reduction in coercive field was observed for BT-Li films. Therefore, this first hypothesis associated to the substitution of Ba or Ti by Li is discarded given the results of the present study. These observations, combined with the structural considerations based on the Goldschmidt tolerance factor, lead us to discard the initial hypothesis of Ba^{2+} or Ti^{4+} substitution by Li^{+} as the primary mechanism in our study.

3.4.2. Li additive as a fluxing agent:

the Li additive may alternatively act as a fluxing agent, forming a secondary phase that promotes grain growth at temperatures well below $BaTiO_3$ conventional sintering range of 1200-1400 °C. Indeed, the microscopy observations (SEM, TEM/ STEM) and analysis (EDS) of this study revealed intergranular separate phase, suggesting Li predominantly existing as a separate, likely molten, Li_2CO_3 phase at the grain boundaries.

Li_2CO_3, with its low melting temperature, is considered as dissociated into Li_2O above 700 °C in atmospheric conditions, as described by the reaction:

$$Li_2CO_{3\,(l)} \rightarrow Li_2O_{(s)} + CO_{2\,(g)} \qquad \text{(Eq. 3)}$$

The exact melting and decomposition temperatures for Li_2CO_3 are controversial. However, it was demonstrated that Li_2CO_3 firstly melts at low temperatures in the range of 700-731 °C [46–48], before undergoing the decomposition reaction described above. Various studies have reported a wide range of decomposition temperatures for Li_2O, with some of them as low as 728 and 770 °C [49,50], and others as high as 900 °C [51]. This discrepancy is often attributed to differing experimental atmospheres, highlighting the significant influence of the gaseous atmosphere on Li_2CO_3 decomposition. A study conducted by Shi et al. under argon gas flow, similar to the annealing conditions used in this study, revealed a two-step decomposition process for Li_2CO_3 , as described by the two following reactions [52]:

$$2Li_2CO_{3\,(l)} \rightarrow Li_4CO_{4\,(l)} + CO_{2\,(g)} \qquad \text{(Eq. 4)}$$

$$Li_4CO_{4\,(l)} \rightarrow 2\,Li_2O_{(s)} + CO_{2\,(g)} \qquad \text{(Eq. 5)}$$

The first decomposition occurs at 727 °C, while the second occurs in a wide range of temperature (780-820 °C), depending on the heating rate.

In the annealing experiments of the present study, performed under an argon flow atmosphere, we postulate that the homogeneously distributed secondary phase observed for the 700 °C annealed BT-Li film is just Li_2CO_3, resulting from the melting/decomposition of this compound.

For the 800-900 °C range, the presence of relatively lower carbon content at grain boundaries suggests partial dissociation and volatilization of Li_2CO_3, as temperature was in a range allowing the decomposition reaction to start. This hypothesis could explain lower carbon content in 800 °C and 900 °C annealed films. However, EDS limited sensitivity to light elements like carbon must also be considered, together with the fact that Li is not detectable by EDS. Furthermore, attempts to detect the Li element by EELS were unsuccessful, indicating a Li content below the detection limit. Therefore, even with the hypothesis of partial decomposition of Li_2CO_3, it is plausible that resulting CO_2 may not have completely left the microstructure, and remained trapped at the grain boundaries, leading to re-carbonation during cooling. This hypothesis aligns with existing literature on the decomposition of Li_2CO_3. Notably, various studies have demonstrated that the diffusion and subsequent release of CO_2 during the melting and decomposition of Li_2CO_3 are prevented by the melting of Li_2CO_3 [53,54]. Additionally, the formed solid Li_2O phase was also reported to the escape of CO_2 [55].

To sum up, the proposition is that the Li_2CO_3 liquid phase formed during annealing is responsible of the enhanced grain growth and the resulting improved electrical properties. This phase, melting at low temperatures (around 700 °C), starts to decompose in the 800-900 °C range. As alkaline oxides in ceramics are known as prone to volatilization, Li is probably vaporized, and subsequently induces a large decrease of Li content. Nonetheless, it remains as a minor element at grain boundaries: Li_2O forms only a minor solid phase that might re-carbonate due to trapped CO_2, eventually reverting to Li_2CO_3 upon cooling. On the other hand, we didn't detect any evidence suggesting the incorporation of Li into the $BaTiO_3$ grains. Thus, we can conclude that Li is not incorporated into the $BaTiO_3$ grains, as the expected effects on microstructure and electrical properties were not observed.

4. Conclusions

The influence of Li_2CO_3 addition on the microstructural and electrical characteristics of aerosol-deposited $BaTiO_3$ thick films was explored. The results reveal that incorporating Li additive into BT films significantly promotes grain growth, thereby reducing the annealing temperature necessary for the restoration of ferro/piezoelectric properties from 800 °C to 650 °C. Furthermore, at relatively high temperatures (≥ 800 °C), grain growth is substantially enhanced, with grain sizes exceeding 200 nm and reaching up to 500-700 nm. This marked increase in grain size is mirrored by notable enhancements in ferroelectric and piezoelectric properties, such as the doubling of remnant polarization (P_r) from 6.6 $\mu A.cm^{-2}$ to 12 $\mu A.cm^{-2}$ for films annealed at 900 °C. In addition to ferro/piezoelectric properties, leakage behavior was also improved, with BT-Li films exhibiting reduced leakage current densities and increased electrical resistivities. The optimal leakage performance was observed at 700 °C, where the leakage current density (j) was measured at 0.1 $\mu A.cm^{-2}$, and the electrical resistivity reached 10^{11} Ω.cm.

Microscopic observations confirmed the probable occurrence of a Li-rich and carbon containing secondary phase at grain boundaries. This phase is likely Li_2CO_3, which melts at 700 °C and begins to dissociate in the 800-900 °C range, together with Li element volatilization. Thus, the Li additive primarily acts as a fluxing agent, facilitating the evolution of microstructure during annealing and contributing to the observed improvements in electrical properties. The results of this study highlight the significant improvement achievable by the use of a low melting point additive in AD-processed piezoelectric films, offering a new way to lower the post-annealing temperatures and optimize the performance of such materials. This strategy can be extended to other lead-free piezoelectric materials as well as to other classical sintering additives.

Declaration of competing interest

The authors declare that they have no known competing financial interests or personal relationships that could have appeared to influence the work reported in this paper.

Acknowledgments

This work is supported by the Nouvelle Aquitaine Region [project AAPR 2021A-2020-12121010] which partially funds Anass Chrir's PhD thesis.

Anass Chrir also benefited from an institutional grant from the National Research with reference ANR-18-EURE-0017 TACTIC.

References

[1] X. Gong, Y.-C. Kuo, G. Zhou, W.-J. Wu, W.-H. Liao, An aerosol deposition based MEMS piezoelectric accelerometer for low noise measurement, Microsyst Nanoeng 9 (2023) 1–13. https://doi.org/10.1038/s41378-023-00484-5.

[2] D.B. Deutz, N.T. Mascarenhas, J.B.J. Schelen, D.M. de Leeuw, S. van der Zwaag, P. Groen, Flexible Piezoelectric Touch Sensor by Alignment of Lead-Free Alkaline Niobate Microcubes in PDMS, Advanced Functional Materials 27 (2017) 1700728. https://doi.org/10.1002/adfm.201700728.

[3] R.A. Dorey, R.W. Whatmore, Electrical properties of high density PZT and PMN–PT/PZT thick films produced using ComFi technology, Journal of the European Ceramic Society 24 (2004) 1091–1094. https://doi.org/10.1016/S0955-2219(03)00542-9.

[4] Q. Zhou, S. Lau, D. Wu, K.K. Shung, Piezoelectric films for high frequency ultrasonic transducers in biomedical applications, Prog Mater Sci 56 (2011) 139–174. https://doi.org/10.1016/j.pmatsci.2010.09.001.

[5] A. Toprak, O. Tigli, Piezoelectric energy harvesting: State-of-the-art and challenges, Applied Physics Reviews 1 (2014) 031104. https://doi.org/10.1063/1.4896166.

[6] P. Luginbuhl, G.-A. Racine, P. Lerch, B. Romanowicz, K.G. Brooks, N.F. de Rooij, P. Renaud, N. Setter, Piezoelectric cantilever beams actuated by PZT sol-gel thin film, Sensors and Actuators A: Physical 54 (1996) 530–535. https://doi.org/10.1016/S0924-4247(95)01196-X.

[7] C.C. Hindrichsen, N.S. Almind, S.H. Brodersen, R. Lou-Møller, K. Hansen, E.V. Thomsen, Triaxial MEMS accelerometer with screen printed PZT thick film, J Electroceram 25 (2010) 108–115. https://doi.org/10.1007/s10832-010-9597-4.

[8] D. Kuscer, O. Noshchenko, H. Uršič, B. Malič, Piezoelectric Properties of Ink-Jet–Printed Lead Zirconate Titanate Thick Films Confirmed by Piezoresponse Force Microscopy, Journal of the American Ceramic Society 96 (2013) 2714–2717. https://doi.org/10.1111/jace.12532.

[9] J. Akedo, Room Temperature Impact Consolidation (RTIC) of Fine Ceramic Powder by Aerosol Deposition Method and Applications to Microdevices, J Therm Spray Tech 17 (2008) 181–198. https://doi.org/10.1007/s11666-008-9163-7.

[10] A. Chrir, O. Rojas, L. Boyer, O. Durand-Panteix, P. Marchet, Effect of post-annealing on microstructure and electrical properties of $BaTiO_3$ thick films grown by aerosol deposition (AD), Journal of the European Ceramic Society 44 (2024) 3965–3984. https://doi.org/10.1016/j.jeurceramsoc.2024.01.073.

[11] S. Baba, H. Tsuda, J. Akedo, Thickness dependence of electrical properties of PZT films deposited on metal substrates by laser-assisted aerosol deposition, IEEE Transactions on Ultrasonics, Ferroelectrics, and Frequency Control 55 (2008) 1009–1016. https://doi.org/10.1109/TUFFC.2008.747.

[12] T. Goto, Y. Matsubayashi, J. Akedo, Ceramic coating on rubber by aerosol deposition with cryogenic substrate cooling, Ceramics International 50 (2024) 892–896. https://doi.org/10.1016/j.ceramint.2023.10.173.

[13] Y. Kim, C.-W. Ahn, J.-J. Choi, J. Ryu, J.-W. Kim, W.-H. Yoon, D.-S. Park, S.-Y. Yoon, B. Ma, B.-D. Hahn, Next Generation Ceramic Substrate Fabricated at Room Temperature, Sci Rep 7 (2017) 6637. https://doi.org/10.1038/s41598-017-06774-z.

[14] Y. Matsubayashi, H. Tsuda, T. Nagoshi, J. Akedo, Relationship between dielectric strength and mechanical properties of alumina films fabricated by aerosol deposition, Ceramics International 48 (2022) 28815–28821. https://doi.org/10.1016/j.ceramint.2022.02.008.

[15] Y. Imanaka, J. Akedo, Embedded Capacitor Technology Using Aerosol Deposition, International Journal of Applied Ceramic Technology 7 (2010) E23–E32. https://doi.org/10.1111/j.1744-7402.2009.02359.x.

[16] N.H. Khansur, U. Eckstein, L. Benker, U. Deisinger, B. Merle, K.G. Webber, Room temperature deposition of functional ceramic films on low-cost metal substrate, Ceramics International 44 (2018) 16295–16301. https://doi.org/10.1016/j.ceramint.2018.06.027.

[17] T. Hoshina, Size effect of barium titanate: fine particles and ceramics, Journal of the Ceramic Society of Japan 121 (2013) 156–161. https://doi.org/10.2109/jcersj2.121.156.

[18] V. Buscaglia, C.A. Randall, Size and scaling effects in barium titanate. An overview, Journal of the European Ceramic Society 40 (2020) 3744–3758. https://doi.org/10.1016/j.jeurceramsoc.2020.01.021.

[19] J. Akedo, N. Minami, K. Fukuda, M. Ichiki, R. Maeda, Electrical properties of direct deposited piezoelectric thick film formed by gas deposition method annealing effect of the deposited films, Ferroelectrics 231 (1999) 285–292. https://doi.org/10.1080/00150199908014545.

[20] M. Tsukamoto, M. Mori, S. Baba, N. Abe, J. Akedo, Effect of diode laser irradiation on ferroelectrics properties of PZT fimls produced by aerosol depositon method, in: AIP Publishing, 2004. https://doi.org/10.2351/1.5060376.
[21] S. Baba, M. Lebedev, J. Akedo, N. Abe, CO_2 laser annealing of $Pb(Zr,Ti)O_3$ aerosol-deposition film on stainless-steel-sheet, in: S. Miyake (Ed.), Novel Materials Processing by Advanced Electromagnetic Energy Sources, Elsevier Science Ltd, Oxford, 2005: pp. 249–252. https://doi.org/10.1016/B978-008044504-5/50051-9.
[22] J.J. Choi, J.H. Jang, D.S. Park, B.D. Hahn, W.H. Yoon, C. Park, Electrical Properties of Lead Zinc Niobate - Lead Zirconate Titanate Thick Films Formed by Aerosol Deposition Process, Solid State Phenomena 124–126 (2007) 169–172. https://doi.org/10.4028/www.scientific.net/SSP.124-126.169.
[23] J. Ryu, J.-J. Choi, B.-D. Hahn, D.-S. Park, W.-H. Yoon, K.-H. Kim, Fabrication and ferroelectric properties of highly dense lead-free piezoelectric $(K_{0.5}Na_{0.5})NbO_3$ thick films by aerosol deposition, Applied Physics Letters 90 (2007) 152901. https://doi.org/10.1063/1.2720751.
[24] X.-Y. Wang, C.-Y. Lee, Y.-C. Hu, W.-P. Shih, C.-C. Lee, J.-T. Huang, P.-Z. Chang, The fabrication of silicon-based PZT microstructures using an aerosol deposition method, J. Micromech. Microeng. 18 (2008) 055034. https://doi.org/10.1088/0960-1317/18/5/055034.
[25] S. Baba, J. Akedo, Fiber laser annealing of nanocrystalline PZT thick film prepared by aerosol deposition, Applied Surface Science 255 (2009) 9791–9795. https://doi.org/10.1016/j.apsusc.2009.04.071.
[26] J.-H. Park, Y. Kawakami, M. Suzuki, J. Akedo, Fabrication and Characterization of Optical Micro-Electro-Mechanical System Scanning Devices Using $BaTiO_3$-Based Lead-Free Piezoelectric-Coated Substrate Sheet by Aerosol Deposition, Japanese Journal of Applied Physics 50 (2011) 09ND19. https://doi.org/10.1143/JJAP.50.09ND19.
[27] M. Lebedev, Effects of annealing and poling conditions on piezoelectric properties of $Pb(Zr_{0.52},Ti_{0.48})O_3$ thick films formed by aerosol deposition method, Journal of Crystal Growth (2002).
[28] J. Ryu, J.-J. Choi, B.-D. Hahn, D.-S. Park, W.-H. Yoon, Ferroelectric and Piezoelectric Properties of $0.948(K_{0.5}Na_{0.5})NbO_3$–$0.052LiSbO_3$ Lead-Free Piezoelectric Thick Film by Aerosol Deposition, Applied Physics Letters 92 (2008) 012905–012905. https://doi.org/10.1063/1.2828892.
[29] M. Bentzen, J. Maier, U. Eckstein, J. He, A. Henss, N. Khansur, J. Glaum, Enhanced grain growth and dielectric properties in aerosol deposited $BaTiO_3$, Journal of the European Ceramic Society 43 (2023) 4386–4394. https://doi.org/10.1016/j.jeurceramsoc.2023.03.012.
[30] U. Eckstein, N.H. Khansur, D. Urushihara, T. Asaka, K. Kakimoto, T. Fey, K.G. Webber, Defect modulated dielectric properties in powder aerosol deposited ceramic thick films, Ceramics International 48 (2022) 33082–33091. https://doi.org/10.1016/j.ceramint.2022.07.241.
[31] U. Eckstein, J. Exner, A. Bencan Golob, K. Ziberna, G. Drazic, H. Ursic, H. Wittkämper, C. Papp, J. Kita, R. Moos, K.G. Webber, N.H. Khansur, Temperature-dependent dielectric anomalies in powder aerosol deposited ferroelectric ceramic films, Journal of Materiomics 8 (2022) 1239–1250. https://doi.org/10.1016/j.jmat.2022.05.001.
[32] K. Maruyama, Y. Kawakami, F. Narita, Young's modulus and ferroelectric property of $BaTiO_3$ films formed by aerosol deposition in consideration of residual stress and film thickness, Jpn. J. Appl. Phys. 61 (2022) SN1011. https://doi.org/10.35848/1347-4065/ac7d96.
[33] Y. Kawakami, M. Watanabe, K.-I. Arai, S. Sugimoto, Piezoelectric Properties and Microstructure of $BaTiO_3$ Films on Heat-Resistant Stainless-Steel Substrates Deposited Using Aerosol Deposition, Transactions of the Materials Research Society of Japan 41 (2016) 279–283. https://doi.org/10.14723/tmrsj.41.279.
[34] T. Kimura, Q. Dong, S. Yin, T. Hashimoto, A. Sasaki, S. Aisawa, T. Sato, Synthesis and Piezoelectric Properties of Li, Ca and Mn-codoped $BaTiO_3$ by a Solvothermal Approach, IOP Conf. Ser.: Mater. Sci. Eng. 47 (2013) 012018. https://doi.org/10.1088/1757-899X/47/1/012018.
[35] Q. Lou, X. Shi, X. Ruan, J. Zeng, Z. Man, L. Zheng, C.H. Park, G. Li, Ferroelectric properties of Li-doped $BaTiO_3$ ceramics, Journal of the American Ceramic Society 101 (2018) 3597–3604. https://doi.org/10.1111/jace.15480.
[36] C.A. Schneider, W.S. Rasband, K.W. Eliceiri, NIH Image to ImageJ: 25 years of image analysis, Nat Methods 9 (2012) 671–675. https://doi.org/10.1038/nmeth.2089.
[37] G.K. Williamson, W.H. Hall, X-ray line broadening from filed aluminium and wolfram, Acta Metallurgica 1 (1953) 22–31. https://doi.org/10.1016/0001-6160(53)90006-6.
[38] M. Khan, A. Mishra, J. Shukla, P. Sharma, X-ray analysis of $BaTiO_3$ ceramics by Williamson-Hall and size strain plot methods, AIP Conference Proceedings 2100 (2019) 020138. https://doi.org/10.1063/1.5098692.

[39] R. Naik, J.J. Nazarko, C.S. Flattery, U.D. Venkateswaran, V.M. Naik, M.S. Mohammed, G.W. Auner, J.V. Mantese, N.W. Schubring, A.L. Micheli, A.B. Catalan, Temperature dependence of the Raman spectra of polycrystalline $Ba_{1-x}Si_xTiO_3$, Phys. Rev. B 61 (2000) 11367–11372. https://doi.org/10.1103/PhysRevB.61.11367.
[40] M.B. Smith, K. Page, T. Siegrist, P.L. Redmond, E.C. Walter, R. Seshadri, L.E. Brus, M.L. Steigerwald, Crystal Structure and the Paraelectric-to-Ferroelectric Phase Transition of Nanoscale $BaTiO_3$, Journal of the American Chemical Society 130 (2008) 6955–6963. https://doi.org/doi/10.1021/ja0758436.
[41] T. Sakashita, M. Deluca, S. Yamamoto, H. Chazono, G. Pezzotti, Stress dependence of the Raman spectrum of polycrystalline barium titanate in presence of localized domain texture, Journal of Applied Physics 101 (2007) 123517. https://doi.org/10.1063/1.2747217.
[42] T. Miyoshi, Preparation of Full-Dense $Pb(Zr,Ti)O_3$ Ceramics by Aerosol Deposition, Journal of the American Ceramic Society 91 (2008) 2098–2104. https://doi.org/10.1111/j.1551-2916.2008.02422.x.
[43] W. Cao, C.A. Randall, Grain size and domain size relations in bulk ceramic ferroelectric materials, Journal of Physics and Chemistry of Solids 57 (1996) 1499–1505. https://doi.org/10.1016/0022-3697(96)00019-4.
[44] T. Hoshina, T. Furuta, Y. Kigoshi, S. Hatta, N. Horiuchi, H. Takeda, T. Tsurumi, Size Effect of Nanograined $BaTiO_3$ Ceramics Fabricated by Aerosol Deposition Method, Jpn. J. Appl. Phys. 49 (2010) 09MC02. https://doi.org/10.1143/JJAP.49.09MC02.
[45] D. Damjanovic, Chapter 4 - Hysteresis in Piezoelectric and Ferroelectric Materials, in: G. Bertotti, I.D. Mayergoyz (Eds.), The Science of Hysteresis, Academic Press, Oxford, 2006: pp. 337–465. https://doi.org/10.1016/B978-012480874-4/50022-1.
[46] L. Ahamad, S.K. Rakshit, S.C. Parida, Y.P. Naik, G.A. Rama Rao, S.G. Kulkarni, S.G. Singh, S.C. Gadkari, Solid-state synthesis and heat capacity measurements of ceramic compounds $LiAlSiO_4$, $LiAlSi_2O_6$, $LiAlSi_3O_8$, and $LiAlSi_4O_{10}$, J Therm Anal Calorim 112 (2013) 17–23. https://doi.org/10.1007/s10973-012-2691-x.
[47] S. Licht, Stabilization of STEP electrolyses in lithium-free molten carbonates, (2012). https://doi.org/10.48550/arXiv.1209.3512.
[48] A.A. Bazhenov, V.V. Miklushevskii, I.I. Vatulin, E.N. Kropacheva, A.P. Bidylo, Study of the process of dissociation of lithium carbonate in the presence of aluminum powder, Russ. J. Non-Ferrous Metals 51 (2010) 44–48. https://doi.org/10.3103/S1067821210010086.
[49] P. Pasierb, R. Gajerski, M. Rokita, M. Rekas, Studies on the binary system Li_2CO_3–$BaCO_3$, Physica B: Condensed Matter 304 (2001) 463–476. https://doi.org/10.1016/S0921-4526(01)00502-6.
[50] J.-W. Kim, H.-G. Lee, Thermal and carbothermic decomposition of Na_2CO_3 and Li_2CO_3, Metall Mater Trans B 32 (2001) 17–24. https://doi.org/10.1007/s11663-001-0003-0.
[51] Y. Di, N. Feng, W. Dong, J. Peng, Y. Wang, Study on Thermal Decomposition of Li_2CO_3 in Production of Lithium by VacuumThermal Reduction Process, Nonferrous Metals(Extractive Metallurgy) (2009) 28–30.
[52] L. Shi, T. Qu, D. Liu, Y. Deng, B. Yang, Y. Dai, Process of Thermal Decomposition of Lithium Carbonate, in: J. Lee, S. Wagstaff, G. Lambotte, A. Allanore, F. Tesfaye (Eds.), Materials Processing Fundamentals 2020, Springer International Publishing, Cham, 2020: pp. 107–116. https://doi.org/10.1007/978-3-030-36556-1_10.
[53] V. Berbenni, C. Milanese, G. Bruni, A. Girella, A. Marini, Synthesis of Li_2SnO_3 by solid state reaction and characterization by TG/DSC, XRPD, and MTDSC, J Therm Anal Calorim 113 (2013) 763–767. https://doi.org/10.1007/s10973-012-2797-1.
[54] A.P. Surzhikov, A.M. Pritulov, E.N. Lysenko, A.N. Sokolovskii, V.A. Vlasov, E.A. Vasendina, Dependence of lithium–zinc ferrospinel phase composition on the duration of synthesis in an accelerated electron beam, J Therm Anal Calorim 110 (2012) 733–738. https://doi.org/10.1007/s10973-011-1947-1.
[55] A.N. Timoshevskii, M.G. Ktalkherman, V.A. Emel'kin, B.A. Pozdnyakov, A.P. Zamyatin, High-temperature decomposition of lithium carbonate at atmospheric pressure, High Temp 46 (2008) 414–421. https://doi.org/10.1134/S0018151X0803019X.